CSMA 2026
17ème Colloque National en Calcul des Structures
18-22 Mai 2026, Presqu'île de Giens (Var)

Data-driven reduced modeling of pleural pressure

F. Álvarez-Barrientos[1], Q. G. Herszkowicz[2,3], A. Duwat[2], D. Rodriguez[2], M. Genet[1]

[1] *Laboratoire de mécanique des solides, CNRS, École polytechnique, Institut Polytechnique de Paris, Palaiseau, France*
[2] *BioMaps, CEA, CNRS, Inserm, Université Paris-Saclay, Orsay, France*
[3] *Siemens Healthcare SAS, Courbevoie, France*

Résumé — Pulmonary digital twins could enhance clinical diagnosis and treatment, but still rely on simplified boundary conditions for mechanical simulations. To address this, we build a pleural pressure model based on dynamic MRI, using a poromechanical approach. We apply high-order SVD to pleural pressure estimated from multiple volunteers to extract spatial and temporal modes, and to quantify their separability. This reduced model will help to identify the physical variables that determine pleural pressure, supporting the development of more physiologically realistic boundary conditions.
Mots clés — pleural pressure, poromechanical modeling, lung MRI, high-order SVD.

1 Introduction

Current trends in computational medicine aim to build digital twins that combine clinical data and physical models to better characterize the state of patients, potentially improving diagnosis and treatment. The complex architecture and mechanics of the lung have attracted significant attention, leading to various modeling approaches to better understand respiratory function [13, 20]. Models have addressed diseases such as idiopathic pulmonary fibrosis [4, 18, 23, 24] and optimized lung ventilation strategies [28] to slow acute respiratory distress syndrome (ARDS). Clinical applications include predicting inhaled drug deposition [3, 21, 22].

Boundary conditions (BCs) for the lung parenchyma remain a major challenge. Most models approximate interactions with the rib cage, diaphragm, and mediastinum through displacement-based assumptions. For example, [24] combined rib cage displacements with frictionless contact and Robin conditions, accurate but computationally demanding. [14] applied homogenization to link micro- and macro-scales, also using Robin conditions, though parameter definitions remain difficult and region-specific. BCs based on nonlinear relations for lung expansion [27] or interpolated CT displacements [15] capture certain dynamics but still oversimplify breathing. Overall, defining physiologically realistic BCs is unresolved.

An alternative is to impose BCs through pleural pressure, which naturally incorporates the effects of surrounding tissue, respiratory muscles, and gravity. It is well known that a pleural pressure gradient exists, which varies in upright, supine and prone positions [16], though exact values and distributions are debated due to measurement challenges. Finite element and CT-based studies highlight the role of gravity, with distinct prone and supine patterns [29]. Reduced models calibrate pleural pressure from imaging and ventilator data [28], but the temporal and spatial analysis is often ignored. More recent porous-medium models incorporate heterogeneous pressures with gravity and thoracic terms [25], reproducing observed deformation gradients but lacking clear physiological basis. To date, no study has analyzed the dynamic evolution together with the regional distribution of pleural pressure.

Most lung models are based on static CT snapshots, usually at end-exhalation and end-inhalation. Advances in MRI now provide time-resolved data, enabling dynamic modeling. Recent developments in 3D MR spirometry [2] have demonstrated the capabilities of obtaining dynamic information from these images, analyzing the lung response during spontaneous breathing. In this article we integrate this type of MRI data, specifically the lung geometry and the registered displacements, into a poromechanical framework [24–26] to estimate pleural pressure fields. Because displacements from MRI inherently reflect the effects of surrounding tissue and respiratory muscles, the resulting pressures fields do so as well. We apply this method to 10 volunteers in the supine position.

While pleural pressure differences between the prone and supine positions are known, their spatio-

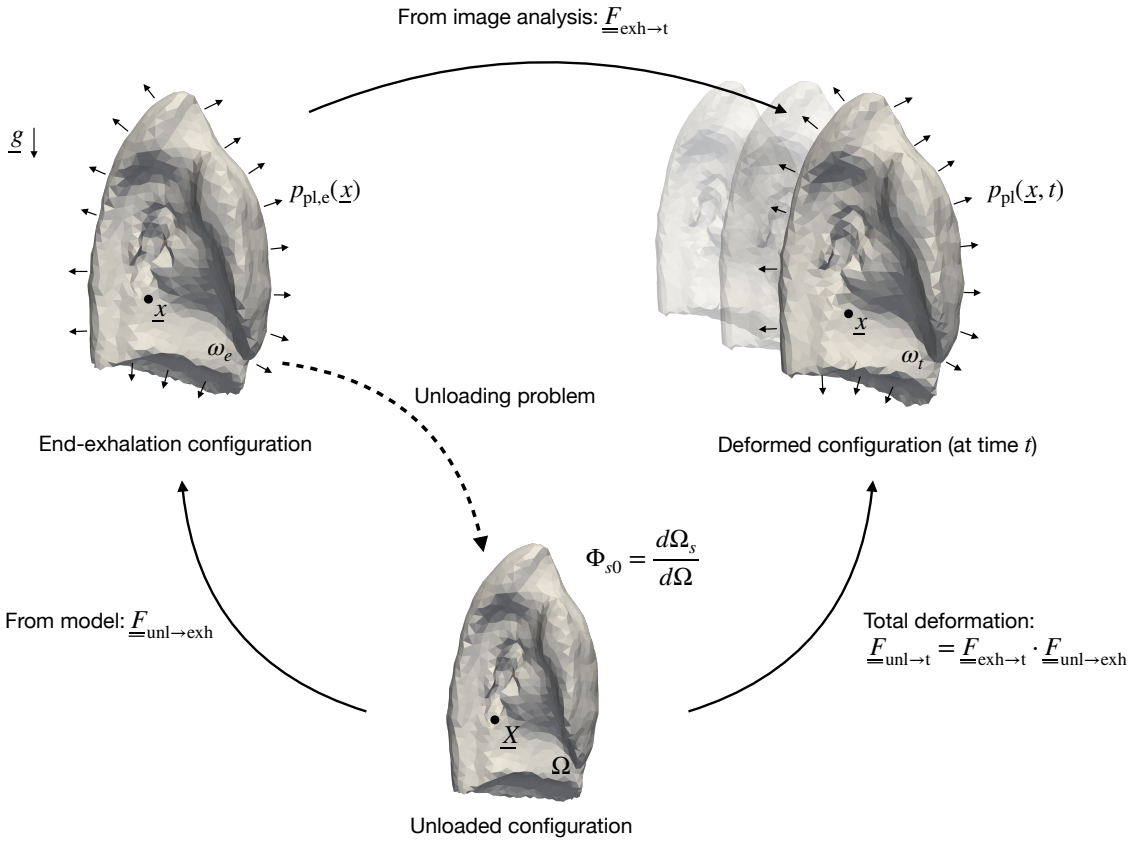

FIGURE 1 – Schema for the estimation of the pleural pressure field at a given time t.

temporal evolution remains poorly described. To study these dynamics, we apply singular value decomposition (SVD), as in prior work in auditory cortex [8] to analyze the separability of the spectro-temporal response. To compare across volunteers, we extend this approach using tools from high-order SVD (HOSVD) [6, 17], enabling simultaneous analysis of the spatio-temporal response in all volunteers. Our goal is to identify recurring patterns, evaluate separability in space and time, and detect breathing modes shared across patients that may reflect underlying physiological mechanisms. The reduced model will also allow us to identify the most relevant variables for a pleural pressure model.

2 Methods

For the lung parenchyma we use the poromechanical model developed by [24, 25], summarized briefly here. This model was originally applied to characterize the lung response from CT images at end-exhalation and end-inhalation. We now adapt it to MR images acquired at multiple stages of the respiratory cycle to estimate the dynamic evolution of pleural pressure. The workflow is :

1. Compute the unloaded configuration, since lungs are already subject to negative pleural pressure (relative to atmosphere) during normal breathing.
2. Use MR-registered displacements and the poromechanical model to compute stresses.
3. Derive tractions on the lung boundary, interpreted as pleural pressure.

A schematic overview is shown in Figure 1. After obtaining the pleural pressure fields for all volunteers, we use HOSVD to evaluate their spatio-temporal separability. From these fields we extract spatial and temporal modes shared across volunteers that capture the pressure dynamics, and we identify which mode combinations are most relevant for each subject. We will then assess how variables such as volume change, maximum pressure, and body position (prone or supine) influence pleural pressure and determine its representation in the reduced model.

2.1 Poromechanical model

The parenchyma is treated as a mixture of a "solid" phase (tissue and blood) and a fluid phase (air). The deformation mapping $\underline{\chi}$ relates a material point $\underline{X}$ in the unloaded configuration Ω to its deformed position $\underline{x}$ in ω, $\underline{\chi} : \underline{X} \to \underline{\chi}(\underline{X}) = \underline{x}(\underline{X})$. Then, the displacement field is $\underline{U}(\underline{X}) := \underline{x}(\underline{X}) - \underline{X}$, and the deformation gradient tensor $\underline{\underline{F}} := \underline{\nabla} \underline{\chi} = \underline{\underline{1}} + \underline{\nabla} \underline{U}$. The volume change of the mixture is $J := \det(\underline{\underline{F}})$. We also define the right Cauchy–Green tensor $\underline{\underline{C}} := \underline{\underline{F}}^T \cdot \underline{\underline{F}}$ and the Green–Lagrange strain tensor $\underline{\underline{E}} := \frac{1}{2}(\underline{\underline{C}} - \underline{\underline{1}})$.

The volume fractions of fluid Φ_f and solid Φ_s are defined as

$$\begin{cases} \Phi_f := \frac{|d\omega_f|}{|d\Omega|} \\ \Phi_s := \frac{|d\omega_s|}{|d\Omega|} \end{cases},$$

with $d\Omega$ an infinitesimal volume of matter of the reference volume Ω, and $d\omega_f$ and $d\omega_s$ infinitesimal volumes corresponding to the fluid and solid phases in the deformed configuration. Subscripts f and s denote fluid- and solid-related quantities, respectively. Additionally, the reference volume fractions are defined as

$$\begin{cases} \Phi_{f0} := \frac{|d\Omega_f|}{|d\Omega|} \\ \Phi_{s0} := \frac{|d\Omega_s|}{|d\Omega|} \end{cases},$$

with $d\Omega_f$ and $d\Omega_s$ being infinitesimal fluid and solid volumes in the reference configuration.

Another important parameter of the model is the added fluid mass per unit reference mixture volume [24], defined as

$$\rho_{f\pm} = \rho_{f0}(\Phi_f - \Phi_{f0}),$$

with ρ_{f0} the reference fluid density and where we assume that the fluid is incompressible.

Let Ψ be the Helmholtz free energy. Following the poromechanical approach [5, 7], we split Ψ into solid and fluid contributions :

$$\Psi(\underline{\underline{E}}, \rho_{f\pm}) = \Psi_s(\underline{\underline{E}}, \Phi_s) + \Psi_f(\Phi_f)$$

where Ψ_s and Ψ_f are the solid and fluid free energies per unit mixture volume in the reference configuration. Note that Ψ_s and Ψ_f can be expressed in terms of $\underline{\underline{E}}, \Phi_s, \Phi_f$ due to the important identities

$$\begin{cases} \Phi_s = J(\underline{\underline{E}}) - \Phi_f \\ \Phi_f = \Phi_{f0} + \frac{\rho_{f\pm}}{\rho_{f0}} \end{cases}.$$

According to the second principle of thermodynamics, the derivative of the free energy with respect to $\underline{\underline{E}}$ gives the second Piola–Kirchhoff stress. Then,

$$\underline{\underline{\Sigma}} = \frac{\partial \Psi(\underline{\underline{E}}, \rho_{f\pm})}{\partial \underline{\underline{E}}} = \underline{\underline{\Sigma}}_s - p_f J \underline{\underline{C}}^{-1},$$

where the "solid" stress is defined as

$$\underline{\underline{\Sigma}}_s := \frac{\partial \Psi_s(\underline{\underline{E}}, \Phi_s)}{\partial \underline{\underline{E}}},$$

and p_f is the internal fluid pressure [24, 25]. From the equilibrium between solid and fluid phases,

$$p_f = -\frac{\partial \Psi_s(\underline{\underline{E}}, \Phi_s)}{\partial \Phi_s}.$$

Additionally, the Cauchy stress tensor can be expressed as

$$\underline{\underline{\sigma}} = J^{-1} \underline{\underline{F}} \cdot \underline{\underline{\Sigma}} \cdot \underline{\underline{F}}^T. \tag{1}$$

Following [24], the solid free energy Ψ_s is decomposed into a component Ψ_{skel} that represents the mechanical behavior of the solid, or skeleton, as a response to deformation, a component Ψ_{bulk} regarding solid volume fraction changes, and a component Ψ_{pore} to ensure positive porosity values. Thus,

$$\Psi_s(\underline{\underline{E}}, \Phi_s) = \Psi_{skel}(\underline{\underline{E}}) + \Psi_{bulk}(\Phi_s) + \Psi_{pore}(\Phi_f).$$

For the definition of these functions, we will use the expressions detailed by [25].

2.2 Unloading problem with imposed unloaded porosity

The unloading step follows [25], assuming the same conditions for the pleural pressure at end-exhalation, with a mean value of -0.5 kPa. A limitation of MRI is that porosity cannot be directly inferred from image intensity (unlike CT, where intensity relates to density). To address this, we assign a uniformly distributed random solid volume fraction in the range $\Phi_{s0} \in [0.4, 0.6]$ in the unloaded configuration. This assumes that, as in the unloaded configuration there are no external forces acting on the lung, such as pleural pressure or gravity, in a healthy volunteer the distribution of solid volume fractions should be approximately uniform. This problem is implemented in an open source finite element code [11] based on the FEniCS library [1, 19] and is available online at https://github.com/mgenet/dolfin_mech.

2.3 Estimation of pleural pressure

To compute the stresses and tractions that represent the pleural pressure, we have to find the deformation from the unloaded configuration to the deformed configuration at each phase t of the respiratory cycle. First, from the unloading problem we compute the displacement $\underline{U}_{unl\to exh}$ and the corresponding $\underline{\underline{F}}_{unl\to exh}$. From MRI analysis we also obtain $\underline{U}_{exh\to t}$ and $\underline{\underline{F}}_{exh\to t}$ for each t. Then, the total deformation from the unloaded configuration to each phase t is

$$\underline{\underline{F}}_{unl\to t} = \underline{\underline{F}}_{exh\to t}\underline{\underline{F}}_{unl\to exh},$$

as represented in the schema of Figure 1. Since volunteers breathe spontaneously, we assume negligible pressure loss between nose/mouth and parenchyma, so $p_f = 0$ (relative to atmosphere). Then $\underline{\underline{\Sigma}} = \underline{\underline{\Sigma}}_s$ and with Equation 1 we can compute the stress. The traction on the boundary is $\underline{t} = \underline{\underline{\sigma}} \cdot \underline{n}$, with $\underline{n}$ the unit normal in the deformed configuration. We assume that the traction on the boundary is due to the pleural pressure, so $\underline{t} \approx (\underline{t} \cdot \underline{n}) \cdot \underline{n}$, which we verified. Each time point t is treated independently, so we can obtain the pleural pressure fields across the respiratory cycle.

2.4 Spatio-temporal analysis

We then compare pleural pressure fields across volunteers. First, for each volunteer the pressure fields obtained throughout the breathing cycle are defined on the lung boundary of the unloaded configuration. To map all subjects to a common reference, we select the unloaded mesh of one of the volunteers and compute transport plans with the POT library [9]. This allows us to translate all pressure fields onto the same mesh.

Let $\underline{\underline{\mathbb{P}}}_{pl,vol}$ be the $n_p \times n_t$ pleural pressure matrix for a volunteer vol, which contains the translated pleural pressure fields on the selected unloaded mesh, where n_t is the number of time frames we have from the MRI and n_p the number of data points (number of faces of the boundary of the selected unloaded mesh). Before applying SVD, for each volunteer and at each phase we subtract the mean pressure at that phase and the component associated with the linear gradient from the hydrostatic pressure distribution within the pleural fluid, $\rho_{pl} g(z - \tilde{z})$, with ρ_{pl} the density of the pleural liquid, g the acceleration of gravity, and $(z - \tilde{z})$ the vertical distance between coordinate z and the center of mass $\tilde{z}$. Let $\underline{\underline{\tilde{\mathbb{P}}}}_{pl,vol}$ be the resulting matrix.

To study the spatio-temporal separability of the pleural pressure, we assemble a 3D array of size $n_t \times n_p \times n_{vol}$, where n_{vol} is the number of volunteers. Following ideas from HOSVD [17], we unfold this array twice : first along the temporal dimension to obtain a matrix of size $n_t \times (n_p \times n_{vol})$, and then along the spatial dimension to obtain a matrix of size $n_p \times (n_t \times n_{vol})$. We perform SVD on each unfolded matrix to obtain the matrices $\underline{\underline{\mathbb{U}}}_t$ and $\underline{\underline{\mathbb{U}}}_{sp}$, whose columns contain the temporal and spatial modes. The singular values from these decompositions indicate the relative importance of each mode.

If we unfold in the n_{vol} direction and apply SVD, we obtain the spatiotemporal modes. While these modes are not the focus here, their singular values allow us to compare the spatial and temporal decompositions with the full spatiotemporal one, and to quantify the degree of spatial and temporal separability in the data.

Let $\underline{f}_i$ be the i-th spatial mode, and $\underline{g}_j$ the j-th temporal mode. With m_{sp} spatial and m_t temporal

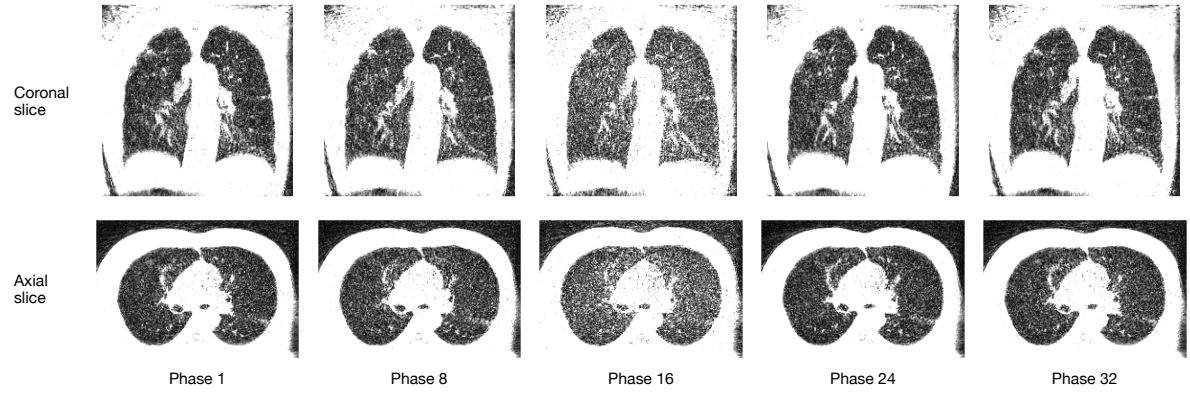

FIGURE 2 – Example of the dynamic MRI data showing five phases of the breathing cycle during spontaneous breathing. Phase 1 corresponds to end-exhalation, and phase 16 corresponds approximately to end-inhalation.

modes, we approximate :

$$\underline{\underline{\tilde{\mathbb{P}}}}_{\mathrm{pl,vol}} \approx \sum_{i=1}^{m_{sp}} \sum_{j=1}^{m_t} \sigma_{ij,\mathrm{vol}} \underline{f_i} \cdot \underline{g_j}^T.$$

To compute $\sigma_{ij,\mathrm{vol}}$, we use the orthonormality of the spatial and temporal modes :

$$\sigma_{ij,\mathrm{vol}} = \underline{f_i}^T \cdot \underline{\underline{\tilde{\mathbb{P}}}}_{\mathrm{pl,vol}} \cdot \underline{g_j}.$$

This decomposition allows us to identify breathing patterns shared across volunteers.

With the spatial and temporal modes and the coefficients $\sigma_{ij,\mathrm{vol}}$, we then assess how well the reduced model reconstructs the original pleural pressure fields. For a given volunteer vol, with m_{sp} spatial and m_t temporal modes, the relative error is

$$\mathrm{err}_{\mathrm{rel}} = \frac{\left| \underline{\underline{\tilde{\mathbb{P}}}}_{\mathrm{pl,vol}} - \sum_{i=1}^{m_{sp}} \sum_{j=1}^{m_t} \sigma_{ij,\mathrm{vol}} \underline{f_i} \cdot \underline{g_j}^T \right|}{\left| \underline{\underline{\tilde{\mathbb{P}}}}_{\mathrm{pl,vol}} \right|}. \tag{2}$$

3 Results

The procedure is applied to data from 10 volunteers in the supine position. MRI were acquired during spontaneous breathing, and the images correspond to 32 phases, obtained as an average over 10 minutes. Figure 2 shows an example of the dynamic MRI data used in this study. To enable direct comparison between subjects, we select the unloaded mesh of volunteer 2 as the reference and transport all pressure fields to this geometry, as shown in Figure 3 at approximately end-inhalation. The responses across volunteers are similar, and a clear dorsal–ventral gradient is observed.

As described in the previous section, once the pleural pressure fields are transported onto the same geometry, we apply HOSVD to analyze separability in time and space. Figure 4a shows the singular values in the spatial, temporal, and spatiotemporal dimensions. A marked drop is visible in the temporal singular values, while the spatial and spatiotemporal values show similar trends. The temporal and spatial modes are shown in Figures 4b and 5, respectively. The first temporal mode remains nearly constant over the respiratory cycle, while the second, third, and fourth modes display sinusoidal variations with different frequencies.

Figure 6 shows the relative error as the number of modes increases. The reconstruction begins with the combination of the first spatial and first temporal modes. Additional spatial modes are then added sequentially up to the fifth. After that, the second temporal mode is included and the process is repeated. For each combination, the pleural pressure field is reconstructed and the relative error is computed at each phase of the breathing cycle using Equation 2. The most influential contribution comes from the first

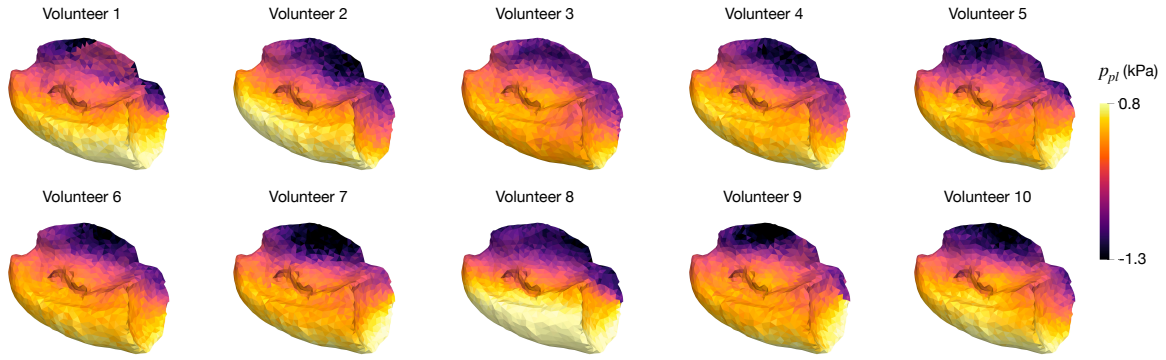

FIGURE 3 – Transported pleural pressure fields at approximately end-inhalation of the 10 volunteers to the selected unloaded mesh of volunteer 2.

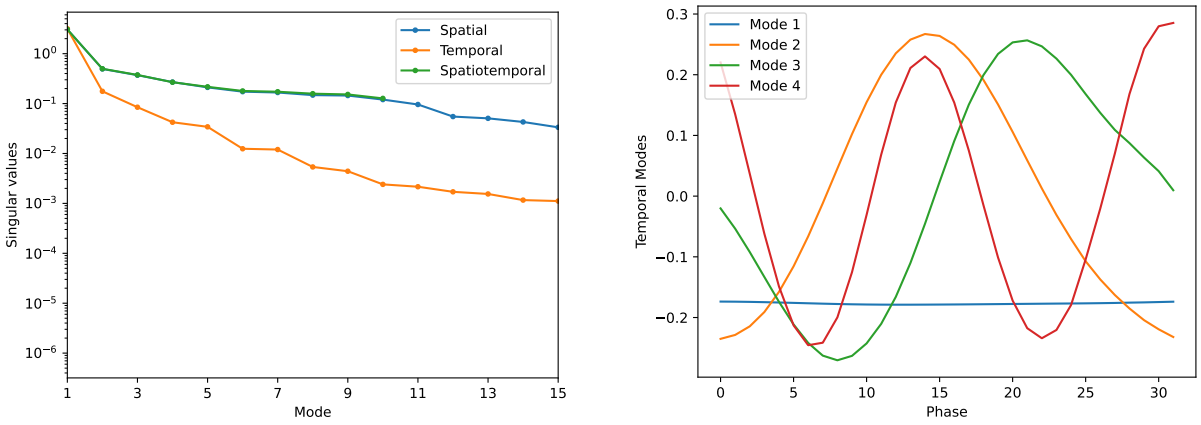

(a) (b)

FIGURE 4 – (a) Singular values from high-order SVD : Spatial, temporal, and spatiotemporal. (b) First 4 temporal modes obtained with high-order SVD.

spatial and first temporal modes, which yield a relative error of roughly 15–35% across volunteers. Some volunteers show additional improvement when the second or third spatial modes are combined with the first temporal mode, while others do not exhibit a meaningful reduction in error with the combinations tested.

4 Discussion

We developed a framework to estimate pleural pressure from MR data and to analyze its spatio-temporal behavior. This provides new insight into pleural pressure dynamics, and the values can be contrasted with reported experimental data [16]. Furthermore, once the results in the prone position are included, it will also be possible to compare our findings with earlier work on regional pressure distributions [29], extending those comparisons to include the temporal evolution.

The HOSVD analysis allows us to assess spatial and temporal separability. If the data were not separable, a combination of spatial and temporal modes would be insufficient, and spatiotemporal modes capturing nonlinear interactions between space and time would be required. In that case, the singular values in the spatiotemporal unfolding would decay faster than those in the spatial or temporal unfoldings. In our results, however, Figure 4a shows that the decay of the spatial and spatiotemporal singular values is similar. This indicates that the data are effectively separable, and that spatial and temporal modes can reconstruct the fields with performance comparable to spatiotemporal modes.

We obtain spatial and temporal modes that characterize the pleural pressure among volunteers. As shown in Figure 6, the first spatial and temporal modes form the most relevant combination for all volunteers. Additional modes affect individuals differently. For example, the third spatial mode paired

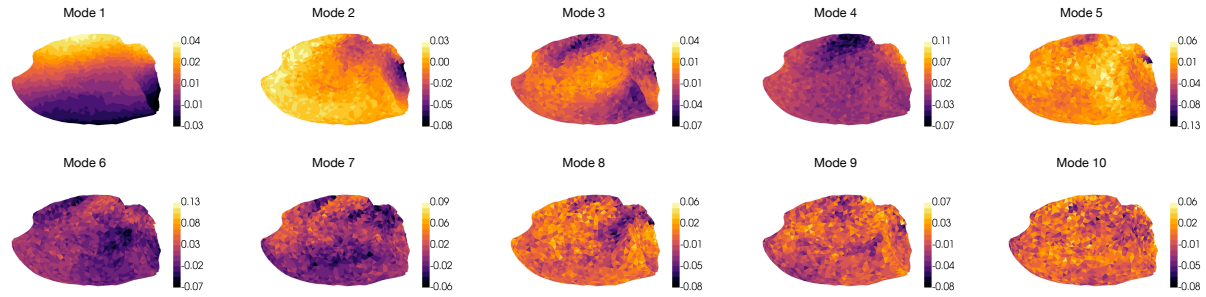

FIGURE 5 – First 10 spatial modes obtained with high-order SVD.

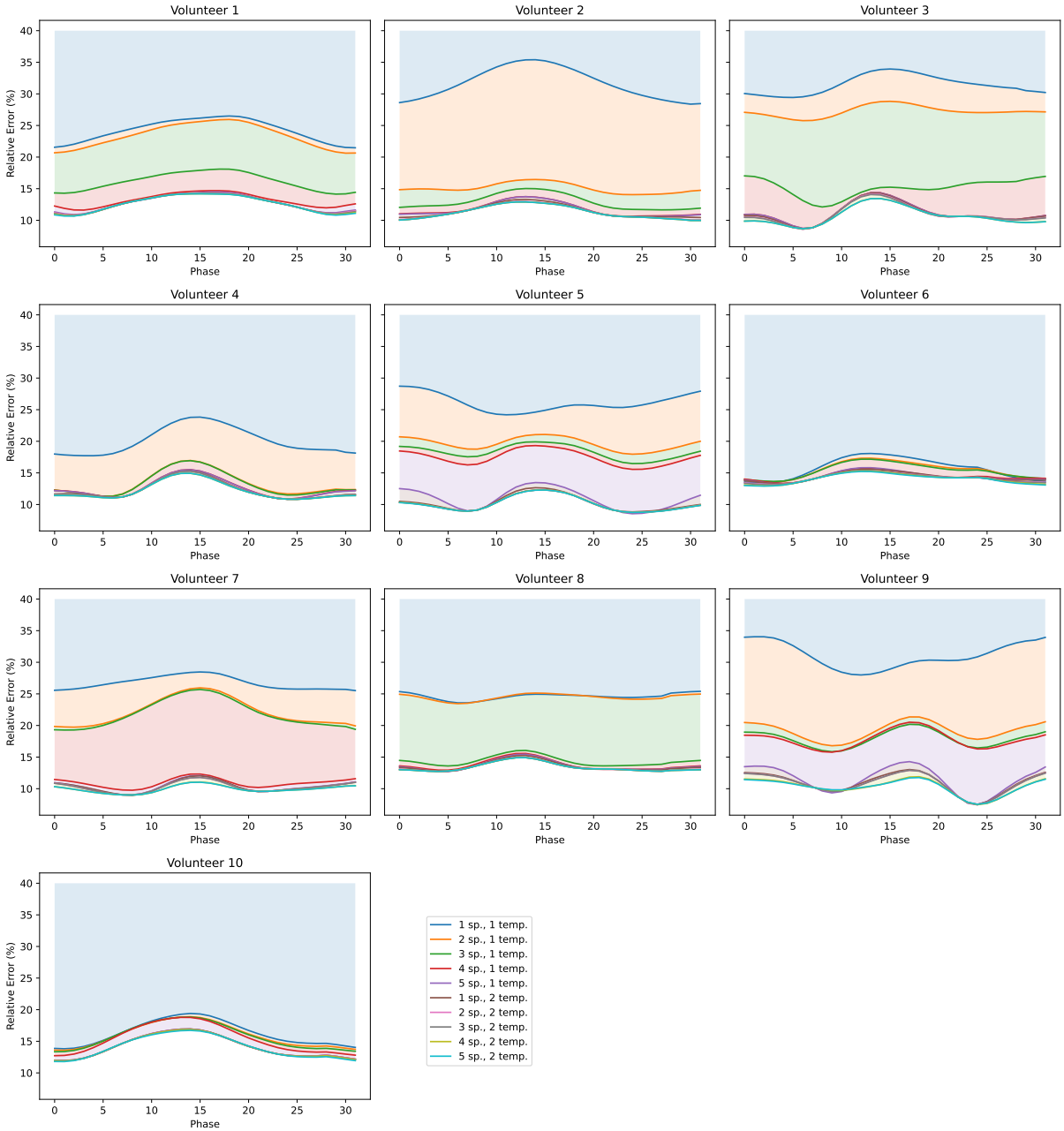

FIGURE 6 – Relative reconstruction error as mode combinations are added. The process starts with the first spatial and first temporal modes, then sequentially includes additional spatial modes and later the second temporal mode. After each added combination, the pleural pressure field is reconstructed and the relative error is recalculated.

with the first temporal mode provides improvements for volunteers 1, 3, and 8. This suggests that certain physiological or geometric factors may influence which modes become relevant. It will be important to examine whether variables such as volume change, peak pressure, or body position (prone or supine) explain these patterns.

Beyond characterization, these pleural pressure maps and the associated spatio-temporal analysis offer a path toward defining more physiologically realistic boundary conditions for lung simulations. Because the fields are derived from measured lung deformation, they implicitly include the mechanical influence of the rib cage, diaphragm, and mediastinum, without requiring explicit models of these structures. With additional data and analysis, it may become possible to determine which physical variables govern the pressure fields and ultimately to construct a physical model for pleural pressure.

Several limitations remain. Porosity cannot yet be robustly estimated from MR images, forcing us to assume a uniform distribution for Φ_{s0}. Improving its estimation across the respiratory cycle would allow patient-specific porosity maps, reducing dependence on this assumption. Furthermore, with porosity information it would be possible to relax the $p_f = 0$ assumption and evaluate its validity in capturing physiological behavior.

For transporting pleural pressure fields to a common reference geometry, we used the POT library. While this method does not guarantee diffeomorphic transformations, the transported fields (Figure 3) remain consistent with the originals. Alternative registration approaches [10, 12] may be explored in future work.

5 Acknowledgments

We thank the funding of the European Union Horizon Europe Research and Innovation Program for V|LF-Spiro3D (Grant Number : 101099934).

Références

[1] M. Alnæs, J. Blechta, J. Hake, A. Johansson, B. Kehlet, A. Logg, C. Richardson, J. Ring, M. E. Rognes, and G. N. Wells. The FEniCS Project Version 1.5. *Archive of Numerical Software*, 3(100), Dec. 2015.

[2] N. Barrau, A. Duwat, C. Fetita, K. Sambourg, A. Beurnier, C. Pellot-Barakat, A. Nemeth, B. Fernandez, T. Boucneau, V. Lebon, and X. Maître. Functional patterns of healthy human respiratory dynamics by 3D MR spirometry. *European Radiology*, Aug. 2025.

[3] L. Boudin, C. Grandmont, A. Lorz, and A. Moussa. Modelling and Numerics for Respiratory Aerosols. *Communications in Computational Physics*, 18(3) :723–756, Sept. 2015.

[4] P.-Y. Brillet, A. Peyraut, J.-F. Bernaudin, C. Fetita, H. Nunes, and M. Genet. What is personalized lung poromechanical modeling and how can it improve the understanding and management of fibrotic interstitial lung diseases ? *Expert Review of Respiratory Medicine*, 19(3) :191–194, Mar. 2025.

[5] D. Chapelle and P. Moireau. General coupling of porous flows and hyperelastic formulations—From thermodynamics principles to energy balance and compatible time schemes. *European Journal of Mechanics - B/Fluids*, 46 :82–96, July 2014.

[6] F. Chinesta and P. Ladevèze, editors. *Separated Representations and PGD-Based Model Reduction*, volume 554 of *CISM International Centre for Mechanical Sciences*. Springer, Vienna, 2014.

[7] O. Coussy. *Poromechanics*. John Wiley & Sons, Mar. 2004.

[8] D. A. Depireux, J. Z. Simon, D. J. Klein, and S. A. Shamma. Spectro-Temporal Response Field Characterization With Dynamic Ripples in Ferret Primary Auditory Cortex. *Journal of Neurophysiology*, 85(3) :1220–1234, Mar. 2001.

[9] R. Flamary, N. Courty, A. Gramfort, M. Z. Alaya, A. Boisbunon, S. Chambon, L. Chapel, A. Corenflos, K. Fatras, N. Fournier, L. Gautheron, N. T. H. Gayraud, H. Janati, A. Rakotomamonjy, I. Redko, A. Rolet, A. Schutz, V. Seguy, D. J. Sutherland, R. Tavenard, A. Tong, and T. Vayer. POT : Python Optimal Transport. *Journal of Machine Learning Research*, 22(78) :1–8, 2021.

[10] M. Genet. Finite strain formulation of the discrete equilibrium gap principle : application to mechanically consistent regularization for large motion tracking. *Comptes Rendus. Mécanique*, 351(G2) :429–458, 2023.

[11] M. Genet, C. Patte, F. Álvarez-Barrientos, D. Hurtado, C. Laville, M. Manoochehrtayebi, and A. Peyraut. Dolfin_mech. Zenodo, Jan. 2025.

[12] M. Genet, C. T. Stoeck, C. von Deuster, L. C. Lee, and S. Kozerke. Equilibrated warping : Finite element image registration with finite strain equilibrium gap regularization. *Medical Image Analysis*, 50 :1–22, Dec. 2018.

[13] A. Gonsard, M. Genet, and D. Drummond. Digital twins for chronic lung diseases. *European Respiratory Review*, 33(174), Dec. 2024.

[14] D. E. Hurtado, N. Avilés-Rojas, and F. Concha. Multiscale modeling of lung mechanics : From alveolar microstructure to pulmonary function. *Journal of the Mechanics and Physics of Solids*, 179 :105364, Oct. 2023.

[15] F. Jiang, T. Hirano, C. Liang, G. Zhang, K. Matsunaga, and X. Chen. Multi-scale simulations of pulmonary airflow based on a coupled 3D-1D-0D model. *Computers in Biology and Medicine*, 171 :108150, Mar. 2024.

[16] R. H. Kallet. A Comprehensive Review of Prone Position in ARDS. *Respiratory Care*, 60(11) :1660–1687, Nov. 2015.

[17] T. G. Kolda and B. W. Bader. Tensor Decompositions and Applications. *SIAM Review*, 51(3) :455–500, Aug. 2009.

[18] C. Laville, C. Fetita, T. Gille, P.-Y. Brillet, H. Nunes, J.-F. Bernaudin, and M. Genet. Comparison of optimization parametrizations for regional lung compliance estimation using personalized pulmonary poromechanical modeling. *Biomechanics and Modeling in Mechanobiology*, 22(5) :1541–1554, Oct. 2023.

[19] A. Logg, K.-A. Mardal, and G. Wells, editors. *Automated Solution of Differential Equations by the Finite Element Method : The FEniCS Book*, volume 84 of *Lecture Notes in Computational Science and Engineering*. Springer, Berlin, Heidelberg, 2012.

[20] S. Neelakantan, Y. Xin, D. P. Gaver, M. Cereda, R. Rizi, B. J. Smith, and R. Avazmohammadi. Computational lung modelling in respiratory medicine. *Journal of The Royal Society Interface*, 19(191) :20220062, June 2022.

[21] V. Neiens, E.-M. Hansbauer, T. J. Jaquin, J. K. Peper-Gabriel, P. Mahavadi, M. E. Snyder, M. J. Grill, C. Wurzenberger, A. Konitsiotis, A. Estrada-Bernal, K. Heinig, A. Fysikopoulos, N. Schwenck, S. Grüner, D. Bartoschek, T. Mosebach, S. Kerstan, J. Wrennall, M. Richter, K. Noda, K. Hoetzenecker, J. K. Burgess, R. Tarran, C. Wurzenberger, K.-R. Wichmann, J. Biehler, K. W. Müller, A. Guenther, O. Eickelberg, M. F. Fitzgerald, S. A. Olwill, G. Matschiner, and M. Pavlidou. Preclinical concept studies showing advantage of an inhaled anti-CTGF/CCN2 protein for pulmonary fibrosis treatment. *Nature Communications*, 16(1) :3251, Apr. 2025.

[22] J. M. Oakes, A. L. Marsden, C. Grandmont, S. C. Shadden, C. Darquenne, and I. E. Vignon-Clementel. Airflow and Particle Deposition Simulations in Health and Emphysema : From In Vivo to In Silico Animal Experiments. *Annals of Biomedical Engineering*, 42(4) :899–914, Apr. 2014.

[23] C. Patte, P.-Y. Brillet, C. Fetita, J.-F. Bernaudin, T. Gille, H. Nunes, D. Chapelle, and M. Genet. Estimation of Regional Pulmonary Compliance in Idiopathic Pulmonary Fibrosis Based on Personalized Lung Poromechanical Modeling. *Journal of Biomechanical Engineering*, 144(9) :091008, Sept. 2022.

[24] C. Patte, M. Genet, and D. Chapelle. A quasi-static poromechanical model of the lungs. *Biomechanics and Modeling in Mechanobiology*, 21(2) :527–551, Apr. 2022.

[25] A. Peyraut and M. Genet. A model of mechanical loading of the lungs including gravity and a balancing heterogeneous pleural pressure. *Biomechanics and Modeling in Mechanobiology*, 23(6) :1933–1962, Dec. 2024.

[26] A. Peyraut and M. Genet. Inverse Uncertainty Quantification for Personalized Biomechanical Modeling : Application to Pulmonary Poromechanical Digital Twins. *Journal of Biomechanical Engineering*, 147(081003), June 2025.

[27] N. Pozin, S. Montesantos, I. Katz, M. Pichelin, I. Vignon-Clementel, and C. Grandmont. A tree-parenchyma coupled model for lung ventilation simulation. *International Journal for Numerical Methods in Biomedical Engineering*, 33(11) :e2873, 2017.

[28] M. Rixner, M. Ludwig, M. Lindner, I. Frerichs, A. Sablewski, K.-R. Wichmann, M.-C. Wachter, K. W. Müller, D. Schädler, W. A. Wall, J. Biehler, and T. Becher. Patient-specific prediction of regional lung mechanics in ARDS patients with physics-based models : A validation study. https ://arxiv.org/abs/2408.14607v1, Aug. 2024.

[29] M. H. Tawhai, M. P. Nash, C.-L. Lin, and E. A. Hoffman. Supine and prone differences in regional lung density and pleural pressure gradients in the human lung with constant shape. *Journal of Applied Physiology*, 107(3) :912–920, Sept. 2009.